DOI: 10.1002/ ((please add manuscript number))
Article type: Full Paper

Cholesterol-Derived Mannosylated Polypeptide-Formed Lipid Nanoparticles for Efficient *in Vivo* mRNA Delivery

*Jin-Yue Zeng, Shonya Lingesh, Nithiyaa D/O Bala Krishnan, Brandon Seow Yi Loong, Min Liu, Qingfeng Chen, Yi Yan Yang**

J. Y. Zeng, S. Lingesh, N. D. B. Krishnan, B. S. Y. Loong and Prof. Dr. Y. Y. Yang
Agency for Science, Technology and Research, Bioprocessing Technology Institute, 20 Biopolis Way, Centros #06-01, Singapore 138668, Singapore
E-mail: yyyang@bti.a-star.edu.sg
M. Liu, Q. Chen
Institute of Molecular and Cell Biology, Agency for Science, Technology and Research, 138673, Singapore.

Keywords: lipid nanoparticle, mRNA delivery, mannosylated polypeptide, cholesterol derivative, mannose

Abstract: Effective delivery of lipid nanoparticles (LNPs)-based mRNA vaccines to antigen presenting cells (APCs) is important for eliciting potent immune responses. However, most LNPs-based mRNA vaccines usually suffer from insufficient accumulation in APCs due to the lack of active targeting capability, leading to the limited efficacy and the need for high injection dose. In this study, we synthesized a series of cholesterol-derived mannopolypeptide (CPSM) and cholesterol-conjugated mannose (CM) derivatives to prepare mannosylated LNPs for efficient mRNA delivery. We demonstrated that the co-assembly of CPSM and/or CM with ionizable lipid, helper lipid and cholesterol into LNPs provides the colloidal stability of LNPs, and endows LNPs the ability to target APCs. The leading mannosylated LNPs including CPSM-LNP and CM/CPSM-LNP exhibited efficient mRNA transfection ability in dendritic cells and mice. Specifically, CPSM-LNP and CM/CPSM-LNP showed preferential accumulation in the lymph nodes compared with commercial ALC-LNP from Pfizer/BioNTech's COVID19 mRNA vaccine formultion. This study presents a straightforward yet effective strategy to synthesize cholesterol-derived mannopolypeptides and prepare mannosylated LNPs for successful *in vivo* mRNA delivery.

1. Introduction

Lipid nanoparticles (LNPs) have been developed as the technology platform for the delivery of messenger RNA (mRNA) vaccines, which have shown promising efficacy against COVID-19. [1, 2] mRNA vaccines can encode specific antigenic proteins that stimulate antigen-presenting cells (APCs) to activate the immune responses of B and T cells against various pathogens. [3, 4] Nevertheless, the efficacy of LNPs-based mRNA vaccines is usually limited by insufficient accumulation in APCs, especially dendritic cells (DCs), leading to the requirement of a relatively high injection dose. [5-7] The development of novel LNPs that enable the effective delivery of mRNA vaccines to APCs could significantly improve the efficacy and reduce adverse effects. [8] Recent studies have demonstrated that the assembly of ligand-conjugated lipids into LNPs and the post-modification of LNPs with specific antibodies can endow these LNP formulations with targeting capability. [9] However, the incorporation of antibodies could disrupt the assembly of LNPs due to the potential electrostatic interactions with the ionizable and helper lipids, leading to limited stability and efficacy of mRNA-loaded LNPs (mRNA-LNPs). [10]

The mannose receptor (CD206) is typically highly expressed by the major APCs such as immature DCs and macrophages, which has been extensively explored as the targeting ligand of APCs. [11-14] The use of mannose as the ligand for the targeted delivery of mRNA vaccines to APCs can significantly improve the antigen presentation through MHC I and II molecules. [15] As natural carbohydrates with targeting capability, mannose and its derivatives exhibit unique advantages compared with other targeting ligands such as peptides and antibodies for the functional modification of LNPs, e.g. ease of preparation of mRNA-LNPs and maintaining mRNA stability by mitigating post-functionalization. [16-18] Generally, LNPs are composed of four components: helper lipid, cholesterol, cationic lipid, and PEGylated lipid, which can assemble into a core-shell structure. [19-21] The core consists of the negatively charged nucleic acid that electrostatically interacts with the ionizable lipid. [22] Helper lipid

and PEGylated lipid reside mainly on the surface with a portion of ionizable lipid and cholesterol, forming the shell of LNPs. [23] As the main component, cholesterol can provide the structural integrity of LNPs. [24, 25] Although the co-assembly of mannose-conjugated ionizable and PEGylated lipids into LNPs was reported for improving the uptake of mRNA-LNPs in APCs, [26, 27] the exposed mannose groups on the surface of these LNPs are usually limited. The reason is that while the incorporation of mannose-conjugated cholesterol into LNPs presents the mannose groups on the surface of LNPs, PEG with a long chain on the surface of LNPs hinders the interaction of cholesterol-conjugated mannose with the receptor.

Herein, a series of cholesterol-derived mannopolypeptides (CPSM) was synthesized through controllable ring-opening polymerization (ROP) for the construction of mannosylated LNPs (**Scheme 1A**). This synthetic strategy has significant advantages, including a controllable degree of polymerization, ease to purify and high yields. Furthermore, the incorporation of CPSM and cholesterol-conjugated mannose (CM) into LNPs can enhance the hydrophilicity of the surface of LNPs without PEGylated lipids and facilitate the co-assembly with other lipid components to yield mannosylated LNPs with good size distribution and high colloidal stability (**Scheme 1B-D**). Benefiting from the targeting capability of mannose group, the resulting mannosylated LNPs promote cellular internalization by the DCs, leading to a notable augmentation in transfection efficiency (**Scheme 1E**). Biodistribution studies of mannosylated LNPs *in vivo* further revealed specific accumulation in the lymph nodes compared with the ALC-LNP without mannose groups, which are used in Pfizer/BioNTech's COVID-19 mRNA vaccine (BNT162b2), through subcutaneous injection. Specifically, our mannosylated LNPs exhibited comparable *in vivo* transfection efficiency with the commercial LNPs.

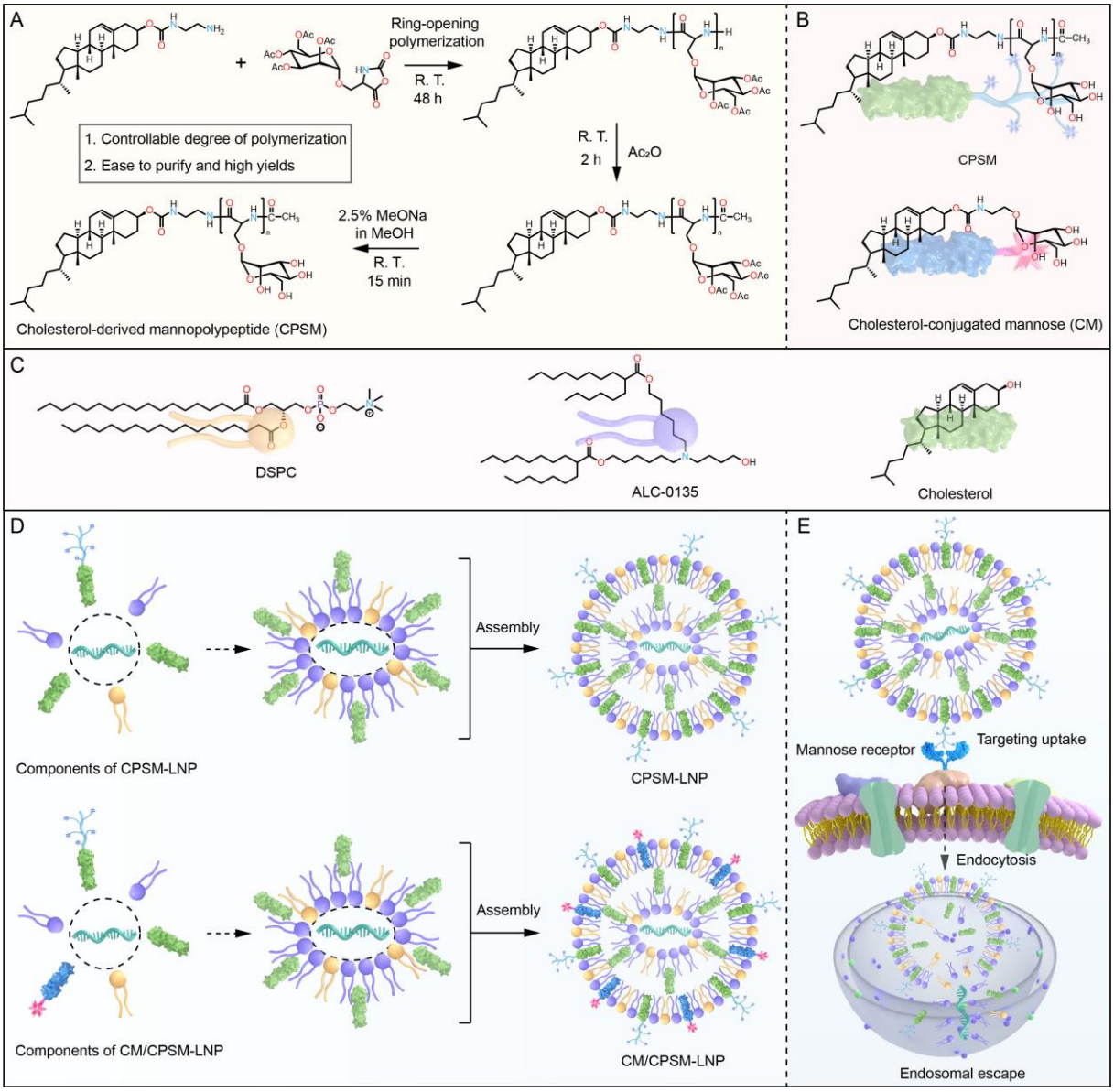

Scheme 1. Schematic illustration of mannosylated LNPs prepared using cholesterol-derived mannopolypeptide mediates efficient mRNA delivery. (A) Synthesis of cholesterol-derived mannopolypeptide (CPSM). (B) Chemical structures of cholesterol-derived mannosylated analogs. (C) Chemical structures of the helper lipid (DSPC), ionizable lipid (ALC-0315) and cholesterol used for LNP formulations. (D) Formulation strategies of CPSM-LNP and CM/CPSM-LNP. (E) Representative mannosylated LNP, CPSM-LNP, for targeted delivery of mRNA to cells that overexpress mannose receptor.

2. Results and Discussion

2.1. Synthesis and Characterization of Cholesterol-Derived Mannopolypeptide (CPSM)

Cholesterol has been demonstrated to enhance the fluidity of gelled membranes, and induce the order to fluid membranes. [28, 29] The inclusion of cholesterol into nanoparticle formulations can promote the endosomal escape and improve the transfection efficiency,

likely due to the enhanced membrane fusion. [30] Based on the function of cholesterol, we designed a series of cholesterol-based mannose derivatives. In this study, cholesterol-conjugated mannose (CM) derivative was first synthesized via the reaction of chloroethyl chloroformate and ethanolamine-1,2,3,4,6-penta-O-acetyl-manno-D-pyranose, followed by deprotection of cholesterol-conjugated 1,2,3,4,6-penta-O-acetyl-manno-D-pyranose (CMO) (**Figure S1**). The successful synthesis of CM and CMO was verified by ^{1}H nuclear magnetic resonance (NMR) spectroscopy (**Figures S2, 3**). Furthermore, cholesterol-derived mannopolypeptide (CPSM) was synthesized *via* the ROP of L-Ser(1,2,3,4,6-penta-O-acetyl-D-mannopyranose)-N-carboxyanhydride (NCA) using the cholesterol-NH_2 derivative as the initiator, followed by the deprotection of cholesterol-derived poly(L-Ser-1,2,3,4,6-penta-O-acetyl-D-mannopyranose) named CPSM-OAc (**Figures S4-8)**. The successful synthesis of CPSM was confirmed by ^{1}H NMR spectroscopy. The ^{1}H NMR spectrum of CPSM clearly showed the peaks of **f-m** and **p** from L-Ser(D-mannose) units and the peak of **a** (-CH_3) from cholesterol at 0.65 ppm, suggesting successful synthesis of CPSM. The disappearance of peaks (-CO-CH_3) indicated successful deprotection of CPSM-OAc. The degrees of polymerization (DPs) of L-Ser(D-mannose) in CPSM can be adjusted by varying the amount of L-Ser(1,2,3,4,6-penta-O-acetyl-D-mannopyranose)-NCA. The DPs of L-Ser(D-mannopyranose) in CPSM were determined by the integration area from the peak **i** of mannopolypeptide and the peak **a** of cholesterol (**Figures S9, 10**). The typical CPSM with different DPs including 6 and 15, were synthesized and denoted as CPSM-6 and CPSM-15, respectively. We also synthesized CPSM-DL-15 through the ROP of L-Ser(1,2,3,4,6-penta-O-acetyl-D-mannopyranose)-NCA and D-Ser(1,2,3,4,6-penta-O-acetyl-D-mannopyranose)-NCA (**Figure S11**).

2.2. Functional Screening of Cholesterol-Derived Mannosylated LNPs

The screening process and *in vitro* studies were designed to investigate physiochemical properties, cellular uptake, endosomal escape and translation of mRNA delivered by

cholesterol-derived mannosylated LNPs (**Figure 1A**). To obtain optimized cholesterol-derived mannosylated LNPs, we evaluated the particle size, size distribution, zeta potential, mRNA encapsulation efficiency, cytocompatibility (cell viability) and *in vitro* mRNA translation efficiency of more than 35 LNP formulations (**Tables S1-3**). For our initial screening, we investigated two cholesterol-conjugated mannose analogs that differ from cholesterol in the head by conjugation of hydrophilic or hydrophobic (protected) mannose groups. We evaluated that whether cholesterol-conjugated mannose analogs supported packaging of mRNA inside LNPs and whether they improved the translation efficiency in DC2.4 cells (DCs, a mouse dendritic cell line). The LNP formulations made using CM (cholesterol-conjugated mannose) and CMO (cholesterol-conjugated mannose with hydrophobic protecting groups) are summarized in **Tables S1**. The size, polydispersity index (PDI), and zeta potential of the mRNA-LNPs were characterized by dynamic light scattering (DLS). These mRNA-LNPs showed nanosize (< 150 nm) with a small PDI (< 0.25) and near neutral zeta potentials (**Figures S12-14**). The encapsulation efficiency of the mRNA-LNPs was determined by the Ribogreen Assay (**Figures S15**). When 5% molar ratio of cholesterol-conjugated mannose analogs were used to replace cholesterol, LNPs formulated with CMO or CM exhibited minor improvement in mRNA transfection in DCs (2.1-fold for CMO, CH-1 and 1.2-fold for CM, CH-6, relative to ALC-LNP, the LNP formulation used in BNT162b2) (**Figure S16**). When the molar ratio of substituted cholesterol increased from 5% (CH-1, CH-6) to 20% (CH-4, CH-9), the translation efficiency decreased (**Figure S16**). Although replacing cholesterol with these two cholesterol-conjugated mannose analogs might increase the uptake of the mRNA-LNPs through mannose-mannose reception interaction, PEG with a long chain on the surface of LNPs could hinder the interaction.

The formulations of cholesterol-derived mannosylated LNPs were further optimized by replacing PEGylated lipid with CPSM (**Table S2**). The optimal amount of CPSM in mannosylated CPSM-LNP was initially determined by using the molar ratio of 1.0-2.0%,

which completely replaced the total amount of PEGylated lipid, ALC-0159. We screened a series of cholesterol-derived mannopolypeptides with different DPs (CPSM-6 and CPSM-15) and optical rotation property (CPSM-DL-15). Most mRNA-LNP formulations prepared using CPSM exhibited small size (< 150 nm), good size distribution (PDI < 0.2), near neutral zeta potential and considerable mRNA encapsulation efficiency (**Figures S17-20**). Notably, LNPs formulated with CPSM are capable of significantly improving translation efficiency of Fluc mRNA in DC2.4 cells as compared to the LNP formulation used in BNT162b2 (ALC-LNP) (**Figure 1B**). This indicated that like PEGylated lipids, CPSM is capable of producing nanosized LNPs. In addition, CPSM-LNP mediated greater mRNA translation efficiency *in vitro*. In particular, mRNA-LNP formed using CPSM-15 at mole ratio of 1.4% showed more than 15 times enhancement in translation efficiency compared to the commercial ALC-LNP formulation in DC2.4 cells.

To make LNPs functionalized with more mannose groups, we screened the CM-LNP without using the PEGylated lipid ALC-0159 by using CM to replace the total amount of cholesterol at mole ratio of 1.6-44.3% (**Table S3**). Meanwhile, we added CM to CPSM-LNP (CPSM-15 at mole ratio 1.4%) to form the CM/CPSM-LNP by replacing cholesterol with CM at mole ratio of 1.6-20%. CM-LNP with CM at the mole ratio from 1.6% to 21.6% were less than 130 nm tested by DLS with low PDI (<0.15) and near neutral surface charge (**Figures S21-23**). However, increasing the molar ratio of CM to 44.3% led to the variation in the size distribution with broad peak in the DLS, and the decrease of mRNA encapsulation efficiency. The addition of CM to CPSM-LNPs had limited influence on the particle size, PDI and zeta potential (CH-18 *vs.* CH-32 to CH-36, **Figures S17-19**, **Figures S21-23**), but it slightly increased the encapsulation efficiency (~65% *vs.* ~80%, **Figure S20, Figure S24**). The mRNA encapsulation efficiencies of CM/CPSM-LNP were comparable with the commercial ALC-LNP (**Figures S24**). All CM-LNP and CM/CPSM-LNP formulations showed a greater translation efficiency compared to the commercial LNPs in DC2.4 cells (**Figures 1C**)

although the addition of CM reduced the translation efficiency (CH-18 in **Figure 1B** vs. CH-31 to CH-36 in **Figure 1C**). Notably, all mRNA-LNPs formulations tested exhibited negligible cytotoxicity, suggesting that cholesterol-derived mannopolypeptides and cholesterol-conjugated mannose derivatives possess good cytocompatibility (**Figures S25-27**). Considering the physiochemical properties, encapsulation efficiency, cell viability and transfection efficacy, we chose the LNP formulations of CH-18 (CPSM-LNP prepared using CPSM-15 at mole ratio of 1.4%), CH-28 (CM-LNP prepared using CM at mole ratio of 11.6%) and CH-35 (CM/CPSM-LNP prepared using CM at mole ratio of 15.0% and CPSM at mole ratio of 1.4%) for further *in vitro* studies. In addition, we tested the colloidal stability of cholesterol-derived mannosylated LNPs at 4 ℃. CPSM-LNP and CM/CPSM-LNP were formulated by microfluidic mixing. CPSM-LNP maintained relatively stable particle size (~100-130 nm), narrow size distribution (PDI < 0.2), no significant change in the zeta potential, and comparable encapsulation efficiency at 4 ℃ for 30 days (**Figure 1D-F**). After 30 days of storage at 4 ℃, CPSM-LNP still showed significantly higher translation efficiency than the commercial ALC-LNP, with negligible cytotoxicity (**Figure S28**). Furthermore, we investigated the changes of hydrodynamic diameter, PDI, zeta potential and encapsulation efficiency of CM/CPSM-LNP at 4 ℃ over time. CM/CPSM-LNP also maintained colloidal stability at 4 ℃ for 30 days without significant changes in the physicochemical properties (**Figures S29-31**). Importantly, compared to fresh ALC-LNP, CM/CPSM-LNP stored at 4 ℃ for 30 days still exhibited substantially higher translation efficiency in DC2.4 cells without cytotoxicity (**Figure S32**). These results revealed that cholesterol-derived mannosylated polypeptide can effectively stabilize the LNP and prevent LNP aggregation.

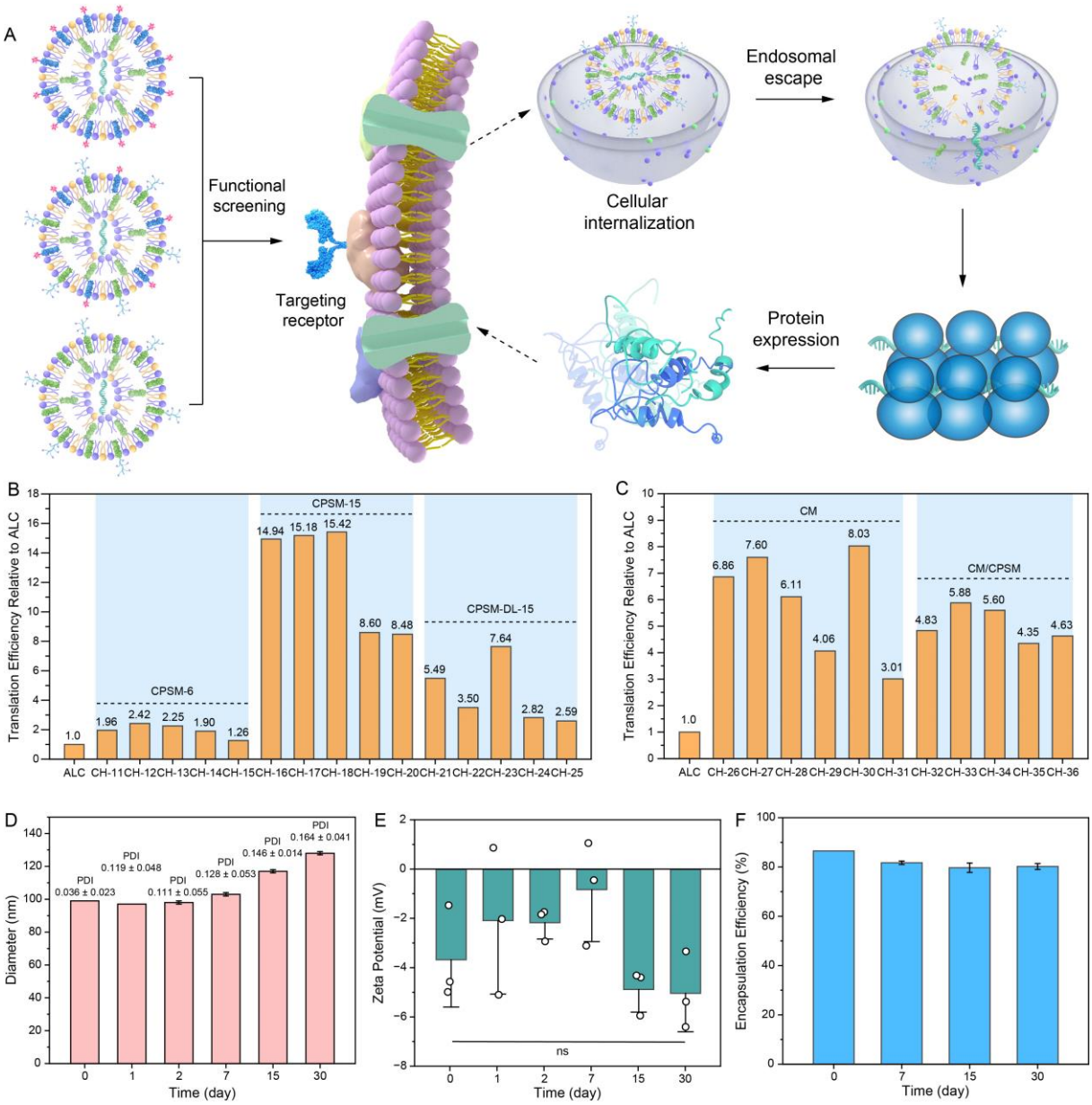

Figure 1. *In vitro* functional screening of cholesterol-derived mannosylated LNPs. (A) Scheme illustrating the investigation on the optimization of mannosylated LNPs. Formulation screening through comparing mRNA translation efficiency in DC2.4 cells of (B) CPSM-LNP prepared using CPSM-15 at mole ratio of 1.4% and (C) CM/CPSM-LNP prepared using CM at mole ratio of 15.0% and CPSM at mole ratio of 1.4%. Colloidal stability analysis of CPSM-LNP at 4 ℃ through (D) hydrodynamic diameter and PDI, (E) zeta potential (ns indicates no significant difference, n = 3), and (F) encapsulation efficiency.

2.3. Microfluidic Formulation and Characterization of Cholesterol-Derived Mannosylated LNPs

Based on the results of formulation screening, we further formulated the optimized mannosylated LNPs including CM-LNP, CM/CPSM-LNP and CPSM-LNP through

microfluidic mixing. The physiochemical characterization of the mRNA-LNPs was performed using DLS. The commercial LNPs (ALC-LNPs) showed small size (~ 70 nm) and low PDI (~ 0.05) (**Figure 2A**). As shown in **Figure 2B-E**, LNPs formulated with CM (CH-28), CPSM (CH-18) or CM+CPSM (CH-35) exhibited nanosize (< 130 nm) with narrow size distribution (PDI < 0.15) and near-neutral zeta potentials (< ± 10 mV). The mRNA-LNPs prepared by microfluidic mixing (especially for CH-28 and CH-35) had relatively smaller sizes compared to those made by manual mixing. This phenomenon was also observed in previous studies. [31] This size decrease is attributed to the fact that microfluidic mixing provides more controlled conditions, allowing for more uniform and efficient mixing of lipids and mRNA, and thus facilitating the self-assembly of smaller, more compact mRNA-LNPs. The nanosize and low PDI of the formulated mRNA-LNPs indicated homogenous particle population, suggesting that the LNPs are viable for efficient cellular uptake and intracellular delivery of the mRNA payload. Furthermore, the near-neutral zeta potential can reduce undesirable non-specific interactions with proteins in the physiological environment and provides *in vivo* stability. The encapsulation efficiency of the mRNA-LNPs was determined through the Ribogreen Assay. LNPs formulated with CM and/or CPSM exhibited comparable encapsulation efficiency with ALC-LNP (**Figure 2F**). High encapsulation efficiency of mRNA in LNPs is critical for effective mRNA delivery as it ascertains a sufficient therapeutic payload that is delivered intracellularly for mRNA expression.

Cholesterol is typically composed of three domains of head, body, and tail. The head of cholesterol is an -OH group, which can interact with the aqueous phase *via* the polarity and hydrogen bonding in liposomal formulations. The body and tail together can facilitate the orderly formation of hydrophobic lipid bilayer. In this work, we used mannopolypeptides and mannose group to replace the hydroxyl groups of cholesterol head groups to enhance the hydrophilicity of cholesterol derivatives (**Figure 2G**). Furthermore, like PEGylated lipids, cholesterol-derived mannopolypeptide provides the stability of LNPs in aqueous solution. The

structure and morphology of CPSM-LNP and CM/CPSM-LNP were characterized by cryo transmission electron microscopy (Cryo-TEM). As shown in **Figure 2H**, mannosylated LNPs formulated with CPSM, CPSM-LNP, displayed a clear core-shell structure, exhibiting a lamellar structure on the nanoparticle surface and a relatively amorphous core. Similar structure and morphology were observed in other LNPs reported by previous studies. [25] Cryo-TEM image of CM/CPSM-LNP also showed a similar structure with CPSM-LNP (**Figure 2I**). These results suggested that the micfluidic mixing of CPSM and/or CM with ionizable lipid, helper lipid and cholesterol can assemble into LNPs with a core-shell structure.

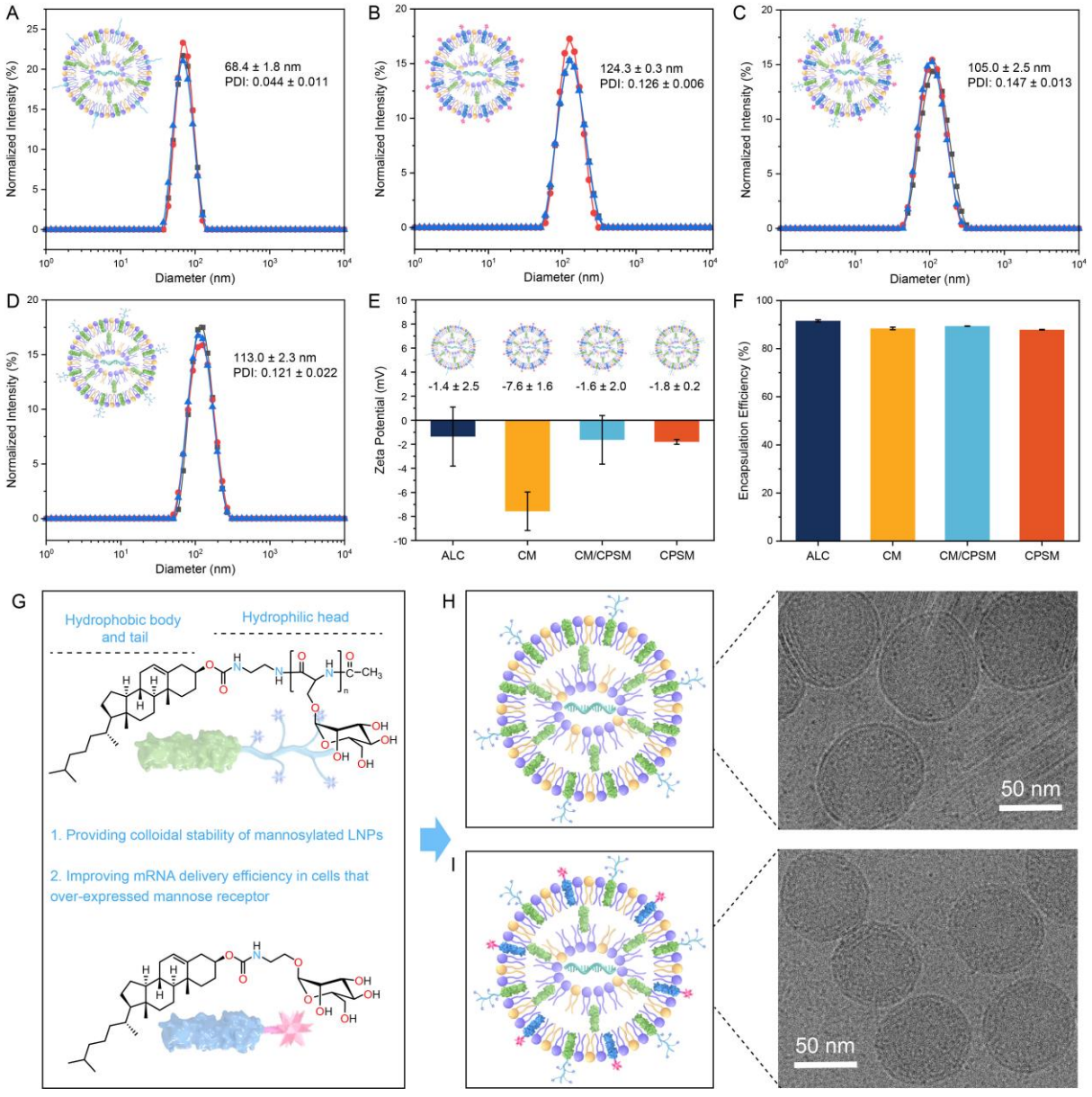

Figure 2. Formulation and characterization of mannosylated LNPs prepared by microfluidic mixing. (A) Particle size distribution of ALC-LNP. (B) Particle size distribution of CM-LNP (CH-28). (C) Particle size distribution of CM/CPSM-LNP (CH-35). (D) Particle size distribution of CPSM-LNP (CH-18). (E) Zeta potential of mannosylated LNPs (n = 3). (F) Encapsulation efficiency of mannosylated LNPs (n = 2). (G) Schematic illustration of the function and effect of cholesterol-derived mannopolypeptide for LNP formulations. (H) Cryo-TEM image of CPSM-LNP. (I) Cryo-TEM image of CM/CPSM-LNP.

2.4. Cellular Internalization and Endosomal Escape of Cholesterol-derived Mannosylated LNPs

Encouraged by the excellent translation efficiency *in vitro*, the cellular internalization and endosomal escape of the optimized mannosylated LNPs (CH-18, CH-28 and CH-35) were further explored through flow cytometry and confocal laser scanning microscope (CLSM). To monitor the cellular uptake and endosomal escape of LNPs in DCs, cyanine5 (Cy5)-labelled mRNA was loaded into LNPs to trace the intracellular translocation. Flow cytometry analysis results revealed that the percentage of Cy5-positive cells treated with mRNA-loaded mannosylated LNPs (~ 98.8% for CM-LNP, ~ 98.3% for CM/CPSM-LNP, ~ 98.7% for CPSM-LNP) increased by about 5% compared with ALC-LNP group (~ 93.4%) (**Figure 3A-E** and **Figure S33**). Notably, the mean fluorescence intensity (MFI) of Cy5-positive cells treated with mRNA-loaded mannosylated LNPs was significantly higher than that of Cy5-positive cells treated with mRNA-loaded ALC-LNP (**Figure 3F**). Specifically, among these three types of mannosylated LNPs, CPSM-LNP exhibited around 4-fold enhancement in MFI compared with ALC-LNP without mannose groups (**Figure 3F**). The efficient internalization of mRNA-loaded mannosylated LNPs could be attributed to the mannose groups on the surface of choleterol-derived mannosylated LNPs. These mannose groups might facilitate effective uptake by DCs that overexpress mannose receptors. CLSM images exhibited cellular internalization of CM/CPSM-LNP loaded with Cy5-mRNA after 2 h of incubation, and the colocalization and separation of red fluorescence from Cy5-mRNA and green fluorescence from lysotracker by extending the incubation time to 6 h (**Figures 3G, 3H**). Furthermore,

CLSM images also showed the separation of red and lysotracker green fluorescence after incubation with CPSM-LNP for 6 h (**Figure 3I**). The colocalization analysis of red fluorescence from Cy5-mRNA and green fluorescence from lysotracker showed the separation of Cy5-mRNA from the endosome after incubation with CPSM-LNP or CM/CPSM-LNP for 6 h, indicating that mRNA-loaded CPSM-LNP and CM/CPSM-LNP were successfully internalized and escaped from the endosomes to cytoplasm. This observation was further supported by analyzing the local colocalization of LNPs and endosomes from the merged confocal images (**Figures S34, S35**). The colocalization analysis of CLSM images indicated that mRNA-loaded CPSM-LNP was successfully escaped from the endosomes to cytoplasm as indicated by the arrows (**Figure S34**). Similar phenomena were also observed in the colocalization analysis of DC2.4 cells treated with CM/CPSM-LNP (**Figure S35**). These results suggested that cholesterol-derived mannosylated LNPs including CPSM-LNP and CM/CPSM-LNP can be used as an mRNA delivery system to obtain efficient translation efficiency in DCs.

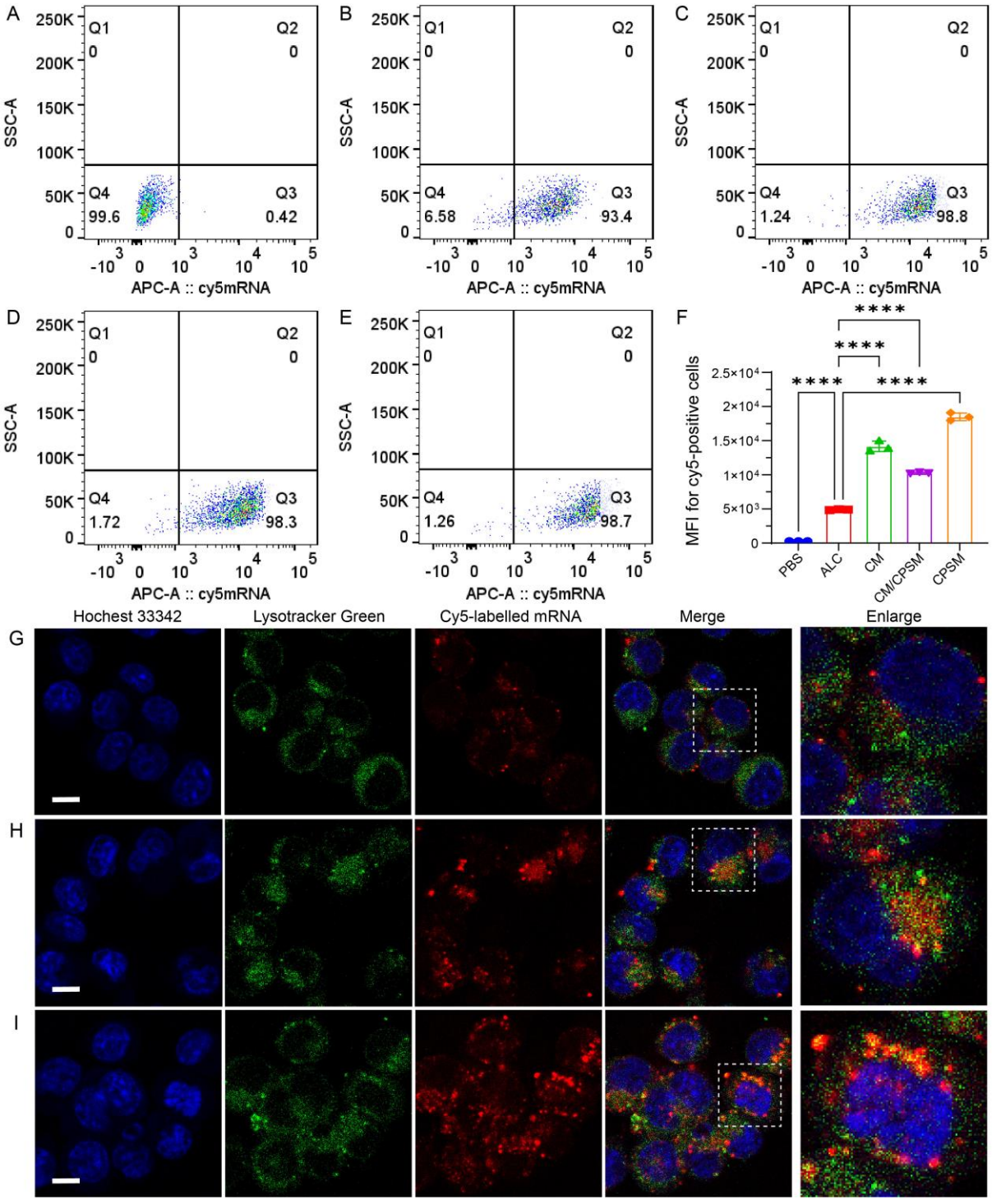

Figure 3. Intracellular delivery and endosomal escape studies of mannosylated LNPs loaded with Cy5-mRNA in DC2.4 cells. Flow cytometry analysis of cellular internalization of (A) control, (B) ALC-LNP, (C) CM-LNP (CH-28), (D) CM/CPSM-LNP (CH-35), and (E) CPSM-LNP (CH18). (F) Uptake efficiency of LNPs containing Cy5-mRNA through flow cytometry analysis (n = 3). CLSM images of DC2.4 cells cultured with (G) CM/CPSM-LNP for 2 h, (H) CM/CPSM-LNP for 6 h, and (I) CPSM-LNP for 6 h. The nuclear were stained by Hochest33342, and the endolysosomes were stained by using LysoTracker Green. Scale bar, 20 μm. ****P < 0.0001.

2.5. *In Vivo* Biodistribution and mRNA Transfection Profiles of Cholesterol-derived Mannosylated LNPs

Inspired by the promising results from *in vitro* studies, we investigated the transfection profiles and biodistribution of CPSM-LNP and CM/CPSM-LNP *in vivo* as aggregation ocurred when we tried to concentrate CM-LNP. In this experiment, the firefly-luciferase (FLuc)-encoded mRNA was used for evaluating the transfection profiles *in vivo*. FLuc mRNA can express firefly luciferase protein that is the enzyme for bioluminescence. After efficient delivery into mice, FLuc mRNA can translate into luciferase protein, which can emit bioluminescence in association with its substrate, luciferin. The bioluminescence distribution studies were performed at 6 h after the subcutaneous injection of FLuc mRNA-loaded LNPs (**Figure 4A**). The penetration depth of bioluminescence is limited, which is why imaging from both the back and front of the mice could provide complementary information. To obtain a more comprehensive view of bioluminescence distribution, we conducted imaging from both angles. We compared the relative bioluminescence radiance intensity (RBRI) of LNPs formulated with FLuc mRNA at the subcutaneous injection site. The bioluminescence images of the back of mice showed that the RBRI of both CM/CPSM-LNP and CPSM-LNP at the injection site was relatively higher than ALC-LNP (used in BNT162b2) (**Figure 4B-4E, Figure 5D**). The bioluminescence imaging from the front of mice provided clearer visualization of bioluminescence distribution in the lymph nodes and other organs (**Figure 4F-4I**). The cholesterol-derived mannosylated LNPs, including CM/CPSM-LNP and CPSM-LNP, not only exhibited efficient mRNA translation at the subcutaneous injection site, but also showed bioluminescence signals in the lymph nodes. The FLuc mRNA-loaded CM/CPSM-LNP and CPSM-LNP successfully transfected mRNA in the lymph nodes with negligible transfection in the liver, which may enhance the immune response of mRNA vaccines while minimizing potential liver toxicity associated with LNPs.

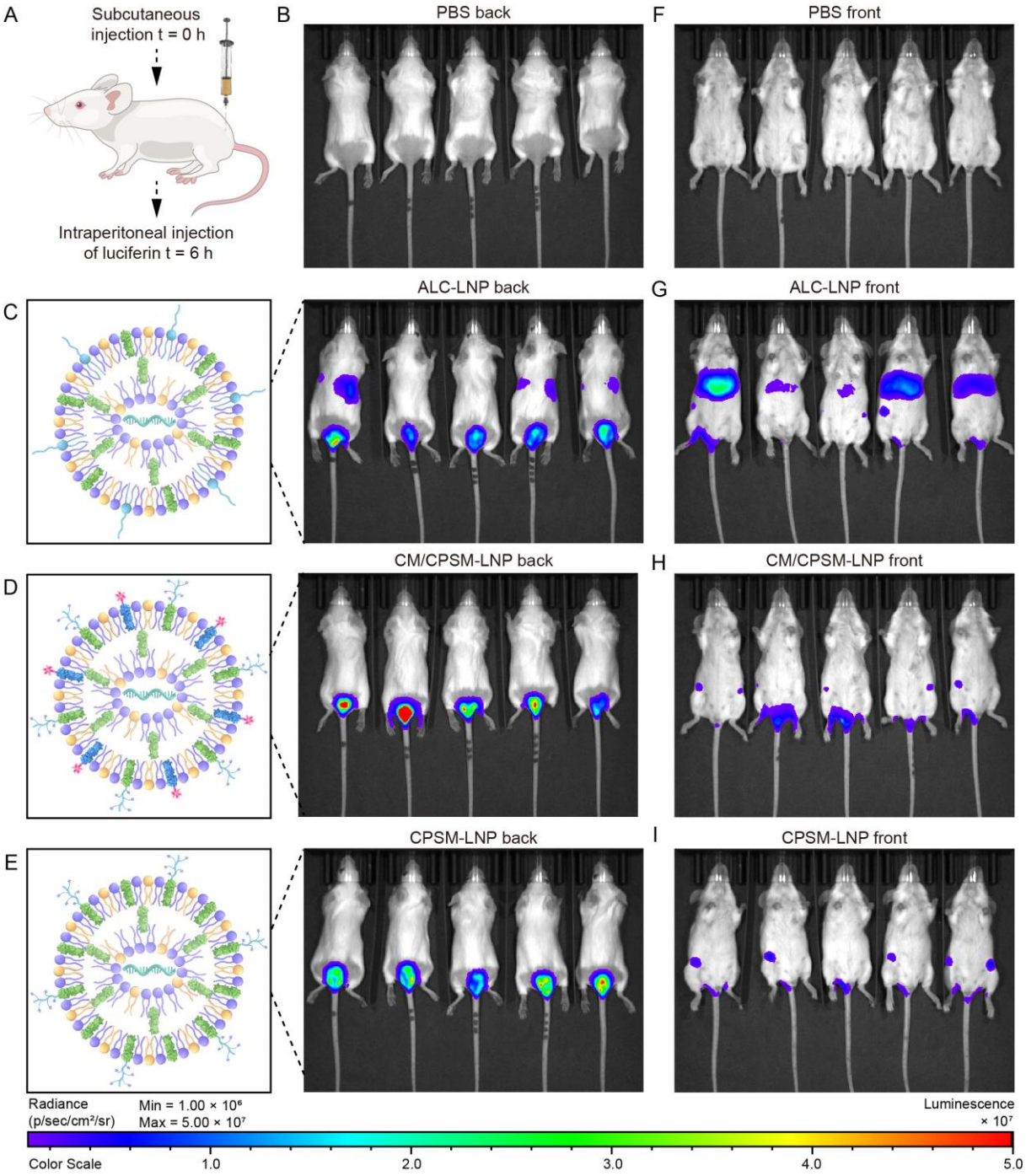

Figure 4. Bioluminescence distribution studies of cholesterol-derived mannosylated LNPs-FLuc mRNA *in vivo*. (A) Scheme illustrating the study of the transfection *in vivo* via subcutaneous injection. Bioluminescence distribution imaging analysis of the back of mice in (B) PBS group, (C) ALC-LNP treated group, (D) CM/CPSM-LNP treated group, and (E) CPSM-LNP treated group. Bioluminescence distribution imaging analysis of the front of mice in (F) control group, (G) ALC-LNP treated group, (H) CM/CPSM-LNP treated group, and (I) CPSM-LNP treated group.

To verify the FLuc mRNA transfection profiles of LNPs in the main organs, we performed *ex vivo* bioluminescence imaging of FLuc mRNA-loaded LNPs for evaluating the

bioluminescence distribution at different organs. The *ex vivo* bioluminescence images of ALC-LNP (used in BNT162b2) showed the clear bioluminescence in both the liver and lymph nodes at 6 h after subcutaneous injection (**Figure 5A**), suggesting that ALC-LNP transfected mRNA effectively and could accumulate in the liver and lymph nodes. Importantly, we found that cholesterol-derived mannosylated LNPs including CM/CPSM-LNP and CPSM-LNP exhibited the preferential bioluminescence distribution in the lymph nodes, suggesting their accumulation in the lymph nodes (**Figure 5B, 5C**). This could be attributed to the incorporation of cholesterol-derived mannopolypeptide into CM/CPSM-LNP and CPSM-LNP, which can improve the uptake of LNPs by immune cells that over express mannose receptor.[11] Furthermore, we compared the RBRI of Fluc mRNA-loaded LNPs including ALC-LNP, CM/CPSM-LNP and CPSM-LNP in the different organs. The RBRI of CPSM-LNP in the lymph nodes was relatively higher than that of ALC-LNP without mannose groups **(Figure 5E**). There was no significant difference in the RBRI in the lymph nodes between CM/CPSM-LNP and ALC-LNP. Notably, the RBRI in the liver of ALC-LNP treated group was significantly higher than that of CM/CPSM-LNP, CPSM-LNP and PBS treated groups **(Figure 5F**, **Figure S36**). There was no significant difference in the RBRI of all Fluc mRNA-loaded LNPs in the heart, lungs and spleen compared with the PBS group **(Figure 5G-I**). Additionally, the RBRI in the kidney of the LNPs-treated groups was higher than that of the control group **(Figure 5J**), which might be attributed to the LNPs being taken up by kidney cells during metabolism.

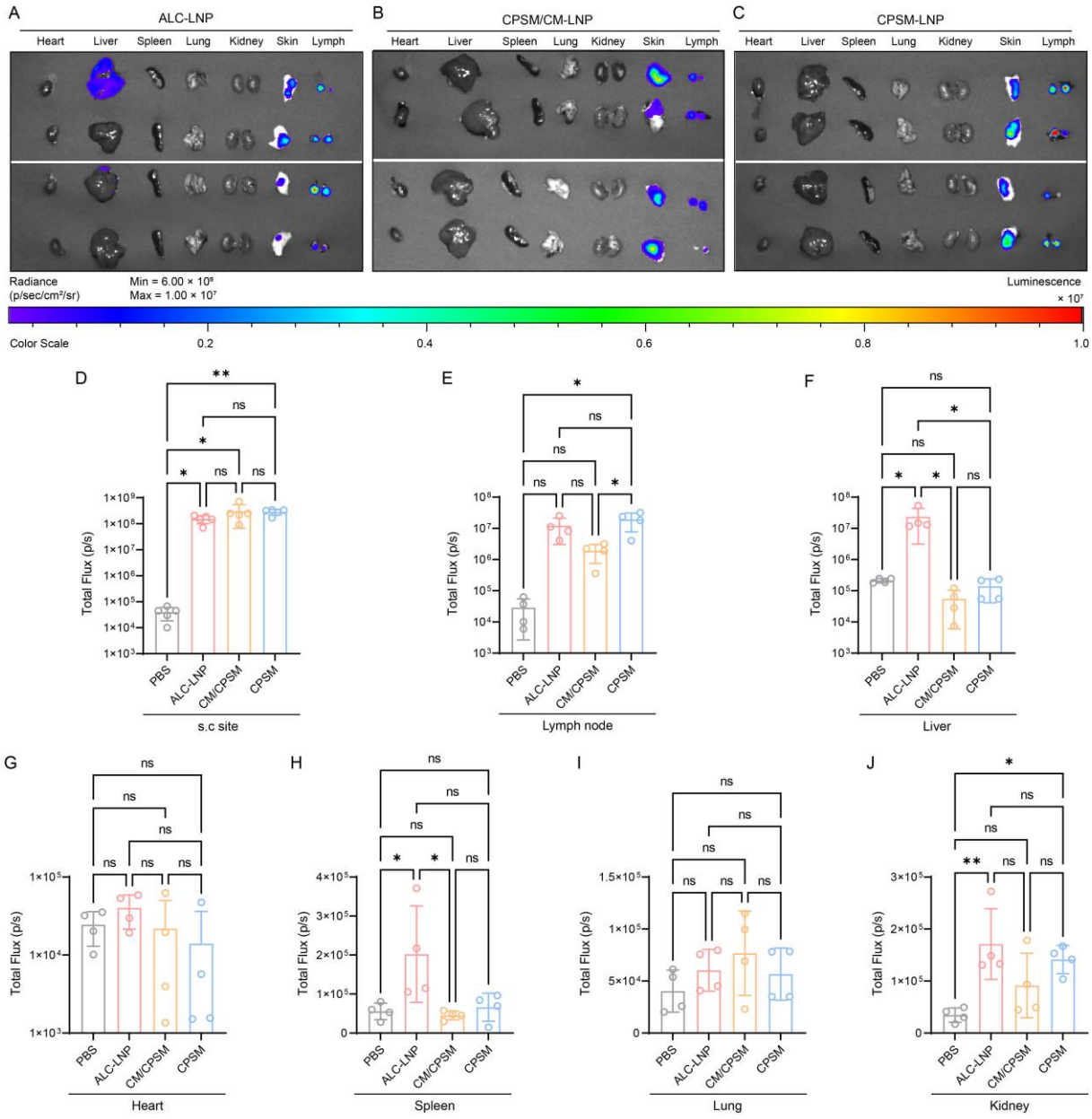

Figure 5. Transfection and biodistribution studies of FLuc mRNA-loaded LNPs through *ex vivo* bioluminescience imaging. Representative images of bioluminescence distribution in each organ of mice treated with (A) ALC-LNP, (B) CM/CPSM-LNP, or (C) CPSM-LNP after 6 h of subcutaneous administration. (D) The relative bioluminescence radiance intensity (RBRI) at the subcutaneous injection site of mice treated with different LNPs after 6 h of subcutaneous administration. RBRI of (E) lymph nodes, (F) liver, (G) heart, (H) spleen, (I) lung, and (J) kidney of mice treated with ALC-LNP, CM/CPSM-LNP or CPSM-LNP after 6 h of subcutaneous administration (ns: no significant difference, *P < 0.05, **P < 0.01, n = 4).

Benefiting from the functionalization of cholesterol-derived mannopolypeptides, both CM/CPSM-LNP and CPSM-LNP exhibited the preferential bioluminescence distribution in the lymph nodes (**Figure 6A**). To further confirm the biodistribution of CM/CPSM-LNP and

CPSM-LNP at different organs, we also carried out the near-infrared fluorescence imaging experiments. The near-infrared dye DIR', DiIC18(7) (1,1'-dioctadecyl-3,3,3',3'-tetramethylindotricarbocyanine iodide), was encapsulated in LNPs with mRNA. DiR'-loaded mRNA-LNPs were injected subcutaneously into mice. The *ex vivo* near-infrared fluorescence images showed that ALC-LNP mainly accumulated in the liver and lymph nodes at 6 h after subcutaneous injection (**Figure 6B, C**). Notably, CM/CPSM-LNP showed specific accumulation in lymph nodes (**Figure 6D).** A similar phenomenon was also observed for CPSM-LNP **(Figure S37**). These are consistent with the results of bioluminescence distribution studies (**Figure 5**). There was no significant difference in the relative fluorescence radiance intensity (RFRI) of the heart, lungs, spleen and kidney of mice treated with CM/CPSM-LNP or CPSM-LNP compared with that in the PBS group (**Figure 6E-F, H-I**). The RFRI of the liver for ALC-LNP treated gorup was significantly higher than CM/CPSM-LNP and CPSM-LNP treated groups as well as the PBS group (**Figure 6F**), while there was no significant difference in the RFRI between CM/CPSM-LNP or CPSM-LNP treated group and the PBS group. All DiR'-loaded mRNA-LNPs showed relatively higher accumulation in the spleen as compared to the PBS group (**Figure 6G**). Furthermore, the RFRI in the lymph node for mannosylated LNPs (especially CM/CPSM-LNP) treated group was relatively higher than that for ALC-LNP treated group (**Figure 6J**). These results demonstrated that CM/CPSM-LNP and CPSM-LNP preferably delivered mRNA to the lymph nodes and spleen as compared to other organs.

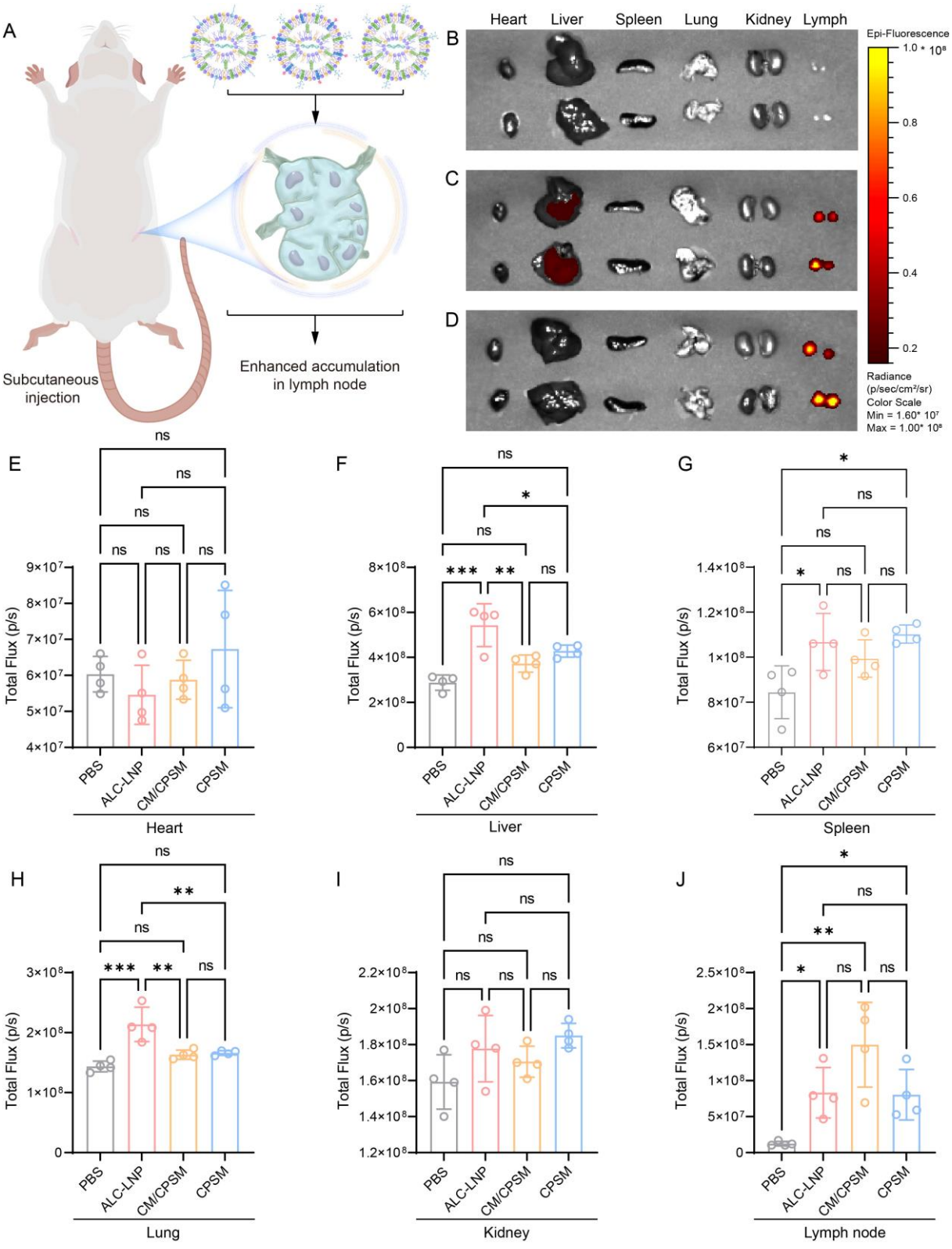

Figure 6. Biodistribution studies of mannosylated LNPs labelled with DiR' through *ex vivo* near infrared fluorescence imaging. (A) Scheme illustrating the enhanced accumulation of mannosylated LNPs in lymph node. Representative images of near infrared fluorescence distribution in each organ of mice in (B) control group, (C) ALC-LNP treated group, and (D) CM/CPSM-LNP treated group after 6 h of subcutaneous administration. The relative near infrared fluorescence radiance intensity (RFRI) in (E) heart, (F) liver, (G) spleen, (H) lung, (I) kidney, and (J) lymph nodes of mice treated with ALC-LNP, CM/CPSM-LNP, or CPSM-

LNP after 6 h of subcutaneous administration (ns: no significant difference, *P < 0.05, **P < 0.01, ***P < 0.001, n = 4).

3. Conclusion

In summary, we have successfully synthesized a series of cholesterol-derived mannopolypeptides for formulating mannosylated LNPs. This synthetic method exhibited controllable degree of polymerization, ease to purify and high yields. LNPs formulated with cholesterol-derived mannopolypeptides or cholesterol-derived mannose showed nanosize with narrow size distribution and high colloidal stability. Specifically, mannosylated LNPs including CPSM-LNP and CM/CPSM-LNP maintained good colloidal stability, encapsulation efficiency and mRNA translation efficacy at 4 ℃ for 30 days. Benefiting from the targeting ability of mannose group, leading mannosylated LNPs showed effective cellular internalization and endosomal escape in dendritic cells, leading to a significant improvement in mRNA translation efficiency. More importantly, both CPSM-LNP and CM/CPSM-LNP exhibited preferential accumulation in the lymph nodes through subcutaneous injection and effective *in vivo* transfection compared with the commercial ALC-LNP. Therefore, the cholesterol-derived mannosylated LNPs represent a promising nanocarrier for mRNA vaccine delivery.

4. Experimental Section

Materials: EZ Cap™ Firefly Luciferase mRNA (5-moUTP) was supplied by ApexBio Technology (Houston, USA). ALC-0315, 1,2-distearoyl-sn-glycero-3-phosphorylcholine (DSPC), cholesterol and ALC-0159 were purchased from MedChemExpress (Monmouth Junction, USA). Sodium acetate was purchased from Sigma-Aldrich (St. Louis, MO, USA). Triton®-X100, Tris-EDTA, and VivoGlo Luciferin (In Vivo Grade) were purchased from Promega (Madison, WI, USA). DIR' was bought from Life Technologies. Vivaspin 20 centrifugal concentrators were obtained from Sartorius (Goettingen, Germany). RPMI 1640

and DMEM cell culture medium were obtained from Gibco, Thermo Fisher Scientific, USA. Quant-iT RiboGreen RNAassay kit was bought from ThermoFisher, USA, One-Glo™ Luciferase Assay System from Promega, USA) and AlamarBlue assay reagent from Life Technologies, USA.

LNP Formulations: To produce the LNPs, varying mole ratios of ALC-0315, DSPC, cholesterol, ALC-0159, CM and CPSM were mixed in ethanol to obtain the organic phase. The molar ratio ALC-LNP is 46.3:9.4:42.7:1.6:0:0. The molar ratio CPSM-LNP is 46.3:9.4:42.7:0:0:1.4. The molar ratio CM-LNP is 46.3:9.4:32.7:0:11.6:0. The molar ratio CM/CPSM-LNP is 46.4:9.4:27.8:0:15:1.4. The aqueous phase was formed by preparing mRNA in sodium acetate buffer (pH 4, 10 mM). Both phases (volume ratio = 3:1) were passed through the NanoAssemblr Ignite benchtop microfluidic device (Precision Nanosystems, Canada) at a fixed flow rate of 12 mL/min to achieve controlled mixing. The nitrogen/phosphate (N/P) ratio (the nitrogen in ALC-0315 to mRNA phosphate groups) was kept constant at 6:1. The resulting mRNA-LNPs were concentrated using a Vivaspin 20 centrifugal concentrator (Mw cutoff = 30 kDa) after undergoing a buffer exchange with Tris buffer). Zetasizer UltraRed (Malvern Panalytical, UK) was used to evaluate the physicochemical characteristics of mRNA-LNPs, including size, PDI and zeta potential. The mRNA-LNP samples were diluted 1:19 in Tris-buffered saline prior to measurement, and a glass cuvette and zeta potential cell were used for analysis.

Sample Preparation and Cryo-TEM Imaging of LNPs: 3.5 µL of LNP samples was applied to a 300-mesh Quantifoil R1.2/1.3 copper grid layered with ultrathin carbon (Quantifoil Micro Tools GmbH) that was glow-discharged in air for 60 s. The grid was then blotted for 2.5 s with blot force 2 at 22 °C and 100% humidity, followed by immediate plunging into liquid ethane using FEI Vitrobot Mark IV. The micrographs were recorded using a 300 kV Titan Krios cryo-transmission electron microscope equipped with a Selectris X imaging filter and a

Falcon 4i direct electron detector. Images were collected at the magnifications of 81,000× or 105,000×, yielding a pixel size of 1.6 Å/px or 1.2 Å/px, respectively.

Encapsulation Efficiency Analysis: The Quant-iT RiboGreen RNA assay kit was utilized to evaluate the encapsulation efficiency and total mRNA concentration. A black, clear-bottom 96-well plate was filled with 10 µL of each mRNA-LNP that had been diluted in Tris-EDTA buffer (pH 8). After that, 90 µL of RiboGreen dye, diluted in Tris-EDTA buffer was pipetted into each well and the plate was incubated in the dark for 20 min. A Spark 10M microplate reader (Tecan, Switzerland) was used to measure the fluorescence intensity (Emission: 480 nm, Excitation: 520 nm). mRNA-LNPs were disrupted using Triton X-100 (0.5% (v/v) to determine the total mRNA concentration. Encapsulation efficiency was calculated by comparing the ratio of RiboGreen fluorescence pre- and post-Triton X-100 treatment.

In Vitro mRNA Transfection: DC 2.4 cells (ATCC, USA) were grown in RPMI-1640 media added with 1% (v/v) Penicillin/Streptomycin and 10% (v/v) FBS. White, clear-bottomed 96-well plates were used to seed the cells. The number of cells plated per well was kept constant at 10,000 cells per well. The cells were given a full day to attach and proliferate prior to LNPs dosage. Each well was then dosed with the mRNA-LNPs in media (100 µL/well) ensuring 100 ng of mRNA per well, and incubated for 48 h at 37 °C and 5% CO_2. One-Glo™ Luciferase Assay System (Promega, USA), was then utilised to evaluate luciferase expression.

Cell Viability Analysis: Black, clear-bottomed 96-well plates were used to seed DC2.4 cells. The AlamarBlue assay was used to assess the cytotoxicity after a 48-hour incubation period with the mRNA-LNPs. The incubation medium was replaced with 100 µL of media containing 10% AlamarBlue reagent. After an additional 2 h of incubation, fluorescence was then measured with the Spark 10M microplate reader (Tecan, Switzerland) at a wavelength of 560/590 nm. The cell viability was then measured by comparing the ratio of florescence of treated and untreated cells.

Cellular Uptake Efficiency Analysis by Flow Cytometry: DC 2.4 cells were seeded in a 12-well plate (20,000 cells per well) and were given a full day to attach and proliferate prior to LNPs dosage. The cells were treated with the Cy5-mRNA-LNPs (200 ng of Cy5-mRNA per well) for 2 h. The cells were subsequently washed with PBS, trypsinized and suspended in 10% FBS-containing PBS. Cell sorting was achieved on a BD LSRFortessa X-20.

Endosomal Escape Studies by CLSM: DC 2.4 cells were seeded in an 8 well Lab-Tek II Chamber Slide at a density of 2×10^4 cells per well for 24 h. Each well was then treated with the mRNA-LNPs in medium (100 µL/well) ensuring 500 ng of Cy5-labelled mRNA per well at N/P ratio of 6. After 6 h, the cells were washed twice with 200 µL of PBS and stained with LysoTracker Green DND-26 (200 nM) for 1.5 h and Hoechst 33342 (10µg/mL) for 20 min. The cells were then washed once again the same way as above and were fixed with 4% paraformaldehyde for 15 min. The cells were examined with a 63× water immersion objective on a Leica Stellaris 8 Falcon (Inverted).

Bioluminescence Imaging Study: The Institutional Animal Care and Use Committee (IACUC) of the Singapore Biological Resource Centre (BRC, approved protocol number: 221681) oversaw all animal procedures. Five to six-week-old female BALB/cAnNTac (BALB/c) mice were acquired from InVivos Pte Ltd (Singapore) and housed in a designated BRC pathogen-free facility. Fifteen BALB/c mice were inoculated with FLuc mRNA-LNPs formulations containing 1 µg of mRNA in 100 µL of TBS via subcutaneous injection at the tail base. Five naive mice injected with luciferin served as a control group. 150 mg/kg of intraperitoneal VivoGlo luciferin (Promega, USA) was given at the specified intervals. After ten minutes, the luminescence signals of mice were recorded using the PerkinElmer IVIS Spectrum imaging system (USA). For *ex vivo* luminescence imaging, the heart, kidney, liver, lungs, inguinal lymph nodes, skin, and spleen were immediately extracted. During the mouse dissection process, the organ of one mouse was lost. To maintain consistency in the number of mice per group, four mice from each group were used for ex vivo bioluminescence imaging

comparison. The Living Image program was used to calculate the overall flux values in each area of interest (PerkinElmer, USA).

Near-Infrared Fluorescence Imaging Study: Fluorescently labelled LNPs were prepared using DiR' from Life Technologies. DiR' at 0.5 mol% (relative to mole of total lipids) was added directly to the organic phase of the LNP formulations before controlled mixing to encapsulate DiR' into LNPs. Similar to the bioluminescence imaging study, subcutaneous injection at the tail base was used to inoculate BALB/c mice with DiR' modified mRNA-LNPs formulations (containing 1 μg of mRNA in 100 μL, n=4). The major organs such as the heart, kidney, liver, lungs, inguinal lymph node, skin, and spleen were immediately extracted. PerkinElmer IVIS Spectrum imaging system (USA) was utilized to acquire the florescence signals of each organ at excitation wavelength of 754 nm and an emission wavelength of 778 nm. The Living Image program was used to calculate the overall flux values in each area of interest (PerkinElmer, USA).

Statistical Analysis: Statistical analysis was performed by using GraphPad Prism 10. Statistical significance was calculated using one-way ANOVA (Analysis of Variance), and data are shown as mean ± SD (ns: no significant difference, *P < 0.05, **P < 0.01, ***P < 0.001, ****P < 0.0001).

Supporting Information

Supporting Information is available from the Wiley Online Library or from the authors.

Acknowledgements

J. Y. Z. and S. L. contributed equally to this work. Z.J.Y. and Y.Y.Y. designed experiments. Z.J.Y. performed synthesis and characterization experiments. J. Y. Z. and S. L. performed functional screening. S. L., N. D. B. K., M. L. Q. C. and Z.J.Y. performed *in vitro* studies. S. L., N. D. B. K., B. S. Y. L. and Z.J.Y. performed *in vivo* experiments. Z.J.Y., S. L. and Y.Y.Y

wrote the manuscript. Y.Y.Y. and J. Y. Z. analyzed and discussed all the data. Y.Y.Y. supervised the study. All authors proofread, commented on, and approved the final manuscript for submission.

This study was financially supported by the Bioprocessing Technology Institute (BTI), Agency for Science, Technology and Research (A*STAR), IAF-PP (H22J1a0050) and NRF-CRP (CRP27-2021-0038), Republic of Singapore.

Conflict of Interest

The authors declare no conflict of interest.

Received: ((will be filled in by the editorial staff))

Revised: ((will be filled in by the editorial staff))

Published online: ((will be filled in by the editorial staff))

References

[1] D. H. Barouch, *N. Engl. J. Med.* **2022**, *387*, 1011.

[2] H. M. E. Sahly, L. R. Baden, B. Essink, S. Doblecki-Lewis, J. M. Martin, E. J. Anderson, T. B. Campbell, J. Clark, L. A. Jackson, C. J. Fichtenbaum, M. Zervos, B. Rankin, F. Eder, G. Feldman, C. Kennelly, L. Han-Conrad, M. Levin, K. M. Neuzil, L. Corey, P. Gilbert, H. Janes, D. Follmann, M. Marovich, L. Polakowski, J. R. Mascola, J. E. Ledgerwood, B. S. Graham, A. August, H. Clouting, W. Deng, S. Han, B. Leav, D. Manzo, R. Pajon, F. Schödel, J. E. Tomassini, H. Zhou, J. Miller, *N. Engl. J. Med.* **2021**, *385*, 1774.

[3] C. L. Lorentzen, J. B. Haanen, O. Met, I. M. Svane, *Lancet Oncol.* **2022**, *23*, e450-e458.

[4] N. Pardi, M. J. Hogan, F. W. Porter, D. Weissman, *Nat. Rev. Drug Discovery* **2018**, *17*, 261.

[5] O. P. Joffre, E. Segura, A. Savina, S. Amigorena, *Nat. Rev. Immunol.* **2012**, *12*, 557.

[6] S. C. Eisenbarth, *Nat. Rev. Immunol.* **2019**, *19*, 89.

[7] M. Vormehr, M. Diken, S. Boegel, S. Kreiter, O. Tureci, U. Sahin, *Curr. Opin. Immunol.* **2016**, *39*, 14.

[8] X. Liu, P. Huang, R. Yang, H. Deng, *ACS Nano* **2023**, *17*, 19550.

[9] J. A. Katakowski, G. Mukherjee, S. E. Wilner, K. E. Maier, M. T. Harrison, T. P. DiLorenzo, M. Levy, D. Palliser, *Mol. Ther.* **2016**, *24*, 146.

[10] P. J. Tacken, I. J. de Vries, R. Torensma, C. G. Figdor, *Nat. Rev. Immunol.* **2007**, *7*, 790.

[11] H. Feinberg, S. A. F. Jégouzo, Y. Lasanajak, D. F. Smith, K. Drickamer, W. I. Weis, M. E. Taylor, *J. Biol. Chem.* **2021**, *296*, 100368.

[12] B. Lepenies, J. Lee, S. Sonkaria, *Adv. Drug Deliv. Rev.* **2013**, *65*, 1271.

[13] F. Mastrotto, M. Pirazzini, S. Negro, A. Salama, L. Martinez-Pomares, G. Mantovani, *J. Am. Chem. Soc.* **2022**, *144*, 23134.

[14] H. Wang, M. C. Sobral, D. K. Y. Zhang, A. N. Cartwright, A. W. Li, M. O. Dellacherie, C. M. Tringides, S. T. Koshy, K. W. Wucherpfennig, D. J. Mooney, *Nat. Mater.* **2020**, *19*, 1244.

[15] J. M. Jaynes, R. Sable, M. Ronzetti, W. Bautista, Z. Knotts, A. Abisoye-Ogunniyan, D. Li, R. Calvo, M. Dashnyam, A. Singh, T. Guerin, J. White, S. Ravichandran, P. Kumar, K. Talsania, V. Chen, A. Ghebremedhin, B. Karanam, A. Bin Salam, R. Amin, T. Odzorig, T. Aiken, V. Nguyen, Y. Bian, J. C. Zarif, A. E. de Groot, M. Mehta, L. Fan, X. Hu, A.

Simeonov, N. Pate, M. Abu-Asab, M. Ferrer, N. Southall, C. Y. Ock, Y. Zhao, H. Lopez, S. Kozlov, N. de Val, C. C. Yates, B. Baljinnyam, J. Marugan, U. Rudloff, *Sci. Transl. Med.* **2020**, *12*, eaax6337.

[16] W. I. Weis, K. Drickamer, W. A. Hendrickson, *Nature* **1992**, *360*, 127.

[17] Q. Fei, E. M. Shalosky, R. Barnes, V. C. Shukla, S. Xu, M. N. Ballinger, L. Farkas, R. J. Lee, S. N. Ghadiali, J. A. Englert, *ACS Nano* **2023**, *17*, 16539.

[18] U. J. Nahar, I. Toth, M. Skwarczynski, *J. Control. Release* **2022**, *351*, 284.

[19] X. Hou, T. Zaks, R. Langer, Y. Dong, *Nat. Rev. Mater.* **2021**, *6*, 1078.

[20] N. Chaudhary, D. Weissman, K. A. Whitehead, *Nat. Rev. Drug Discov.* **2021**, *20*, 817.

[21] X. Han, H. Zhang, K. Butowska, K. L. Swingle, M. G. Alameh, D. Weissman, M. J. Mitchell, *Nat. Commun.* **2021**, *12*, 7233.

[22] J. A. Kulkarni, M. M. Darjuan, J. E. Mercer, S. Chen, R. Van Der Meel, J. L. Thewalt, Y. Y. C. Tam, P. R. Cullis, *ACS Nano* **2018**, *12*, 4787.

[23] J. Viger-Gravel, A. Schantz, A. C. Pinon, A. J. Rossini, S. Schantz, L. Emsley, *J. Phys. Chem. B* **2018**, *122*, 2073.

[24] M. R. Krause, S. L. Regen, *Acc. Chem. Res.* **2014**, *47*, 3512.

[25] S. Patel, N. Ashwanikumar, E. Robinson, Y. Xia, C. Mihai, J. P. Griffith, S. Hou, A. A. Esposito, T. Ketova, K. Welsher, J. L. Joyal, Ö. Almarsson, G. Sahay, *Nat. Commun.* **2020**, *11*, 983.

[26] J. Lei, S. Qi, X. Yu, X. Gao, K. Yang, X. Zhang, M. Cheng, B. Bai, Y. Feng, M. Lu, Y. Wang, H. Li, G. Yu. *Angew. Chem. Int. Ed.* **2024**, *63*, e202318515.

[27] M. Kim, M. Jeong, S. Hur, Y. Cho, J. Park, H. Jung, Y. Seo, H. Woo, K. Nam, K. Lee, *Sci.*

Adv. **2021**, *7*, eabf4398.

[28] W. D. Nes, *Chem. Rev.* **2011**, *111*, 6423.

[29] B. S. Pattni, V. V. Chupin, V. P. Torchilin, *Chem. Rev.* **2015**, *115*, 10938.

[30] Y. Zhuo, Z. Luo, Z. Zhu, J. Wang, X. Li, Z. Zhang, C. Guo, B. Wang, D. Nie, Y. Gan, G. Hu, M. Yu, *Nat. Nanotechnol.* **2024**, https://doi.org/10.1038/s41565-024-01785-0.

[31] S. A. Dilliard, Y. Sun, M. O. Brown, Y. C. Sung, S. Chatterjee, L. Farbiak, A. Vaidya, X. Lian, X. Wang, A. Lemoff, D. J. Siegwart, *J. Control. Release* **2023**, *361*, 361.